

Effect of FCAW Current on the Hardfacing Layer — Microstructure and Wear Resistance

An investigation was conducted to determine optimal binding strength through the effects of flux cored arc welding current on the microstructure, wear resistance, and welding association on the hardfacing layer

BY J. YANG, X. HOU, X. XING, C. WANG, Y. YANG, X. REN, AND Q. YANG

ABSTRACT

The hardfacing layers were deposited with different welding currents. The microstructure was observed by optical microscope (OM), field emission scanning electron microscope (FESEM), and transmission electron microscope (TEM). The phase structure was determined by X-ray diffraction (XRD). Macrohardness and microhardness of the hardfacing layer were determined by a Rockwell hardness tester and a Vickers hardness tester, respectively. The wear resistance was measured by a belt-type wear testing machine. Shear strength between the hardfacing layer and the base metal was determined by an electronic universal testing machine. Subsequently, the temperatures of the hardfacing molten pools were simulated by ANSYS software with three welding currents. The CCT curves of the hardfacing layers were calculated by JMatPro® software during the cooling process. The results indicate that binding strength of the hardfacing layer and the base metal enhances gradually with the increase of the welding current. When the welding current reaches 360–380 A, the binding strength is the highest. With the increases of the welding current, molten pool temperature of the hardfacing layer increases, which improves the hardenability of the hardfacing layer. Therefore, the amount of martensite increases while that of retained austenite decreases, which leads to the increase of the hardness and wear resistance of the hardfacing layer.

mance alloy, which possesses excellent mechanical properties (Ref. 3).

In the surface coating technologies, hardfacing (hard-surface welding) is attracting more and more attention because of its high efficiency, low price, and excellent controllability (Ref. 4). Of all of the hardfacing methods, flux cored arc welding (FCAW) has been used more and more widely because of its high deposition rates and its excellent surface appearance (Refs. 5, 6).

During the welding process, welding parameters directly affect welding performance. C. E. Jackson (Ref. 7) found the welding voltage controls the welding arc length and weld bead width. With an increase of the welding voltage, the welding arc length increases and the weld bead width widens as well. V. Gunaraj (Ref. 8) indicated that, with an increase in travel speed, weld bead penetration and weld bead width both decrease. T. Kannan (Ref. 9) showed that wire feed rate is the most direct factor affecting the morphology of the weld bead. With an increase in the wire feed rate, the deposition rate increases, which leads to an increase in the height and a decrease in the width of the weld bead. Moreover, during the hardfacing process, when the welding parameters are selected incorrectly, weld defects, such as pores, slag inclusions, and cracks, appear on the hardfacing layer (Refs. 10, 11).

Of all the welding parameters,

KEYWORDS

• Hardfacing Layer • Welding Current • Wear Resistance • Numerical Simulation

The hot-rolling supporting roller is a key workpiece during hot-rolling production, because it plays an important role in supporting the work roller. Therefore, the quality of the hot-rolling supporting roller affects not only its service life, but also the quality and production efficiency of hot-rolled products indirectly (Refs. 1, 2).

Although the quality of the hot-rolling supporting roller is certified

when manufactured by integral cast, the cost is high. Therefore, in recent years, the authors attempted to manufacture the hot-rolling supporting roller by a new method. During processing, the core material of the roller is Q235 steel. This material is not only cheap, but also has good toughness, and can be used as a coating layer on a material's surface. The layer material is the self-developed, high-perfor-

J. YANG, X. HOU, X. XING, C. WANG, Y. YANG, and Q. YANG (yangjian0001@126.com) are with the State Key Laboratory of Metastable Materials Science and Technology, College of Materials Science and Engineering, Yanshan University, Qinhuangdao, China. X. REN is with the School of Engineering, Liverpool John Moores University, Liverpool, UK.

welding current is the most important. After performing sensitivity analysis experiments on the welding parameters, S. Karaoglu (Ref. 12) suggested that welding current is the most influential parameter in determining the dimensions of the weld bead penetration and heat-affected zone (HAZ). However, although some scholars have realized the importance of welding current on the welding process, most researchers are focusing their attention on the effect of penetration, the size of the HAZ, joint strength, and so on. Research on the welding current's impact on the microstructure and mechanical properties of the hardfacing layer by FCAW is rare.

In this work, the authors studied three hardfacing layers created by self-developed flux cored wires operated at different welding currents. The effects of welding current on the microstructure, wear resistance, and welding association of the hardfacing layers were analyzed by experiments, numerical simulation, and thermodynamic calculation, which can supply a theoretical foundation for improving the microstructure and properties of the hardfacing layer.

Experiment

Materials and FCAW Processing Parameters

YD-254M flux cored wire, combined with HJ260 flux, which is produced by Beijing Iron and Steel Research Institute, was used in this work. The base metal used was Q235 low-carbon steel, whose composition is listed in Table 1.

In order to analyze the effect of welding current on microstructure and properties of the hardfacing layer, the same welding voltage, travel speed, wire diameter, and tracks overlap were employed with three different welding currents. The welding parameters are listed in Table 2. The composition of the hardfacing layer is given in Table 3.

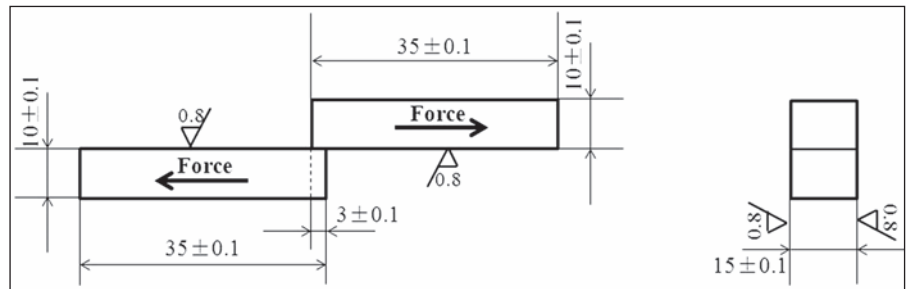


Fig. 1 — Dimensions of the shear testing specimen.

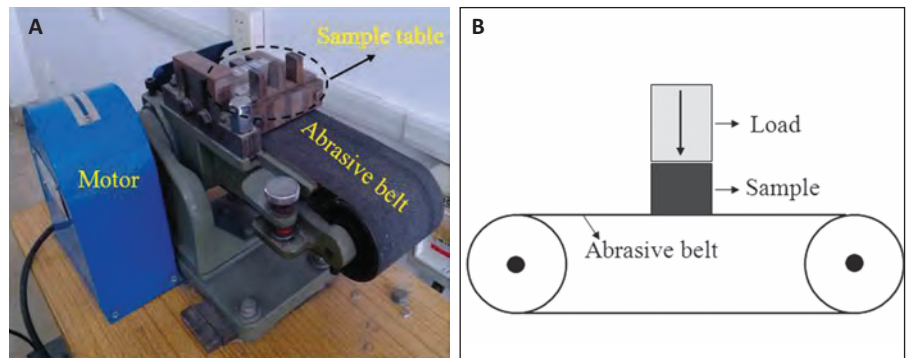


Fig. 2 — Abrasive belt-type wear tester. A — Photograph; B — schematic (Ref. 13).

Microstructure and X-ray Diffraction Characterization

The morphologies of the hardfacing layer and welding joint surface, which were etched with 4% nitric acid alcohol after being metallographically polished, were characterized by an Axiovert 200 MAT optical microscope (OM), Hitachi S4800 field emission scanning electron microscope (FES-

EM), and a Jeolarm-200F transmission electron microscope (TEM).

In order to analyze the phase structure of the hardfacing layer, X-ray diffraction (XRD) of type D/max-2500/PC was undertaken on a diffractometer, using Cu-K α radiation. The samples were scanned from 20 to 120 deg with a step size of 0.02 deg. Each step size was allowed 9 s for X-ray detection.

Table 1 — Chemical Composition of the Q235 Low-Carbon Steel

Elements	C	Mn	Si	S	P	Fe
Content (wt-%)	0.15	0.55	0.30	0.03	0.03	balance

Table 2 — Welding Parameters

Welding Current (A)	Arc Voltage (V)	Travel Speed (mm/min)	Layer Thickness (mm)	Tracks Overlap (%)	Wire Diameter (mm)
200–220	29–30	300	7.5–8.5	45–50	2.8
280–300					
360–380					

Table 3 — Chemical Composition of the Hardfacing Layer

Elements	C	Cr	Ni	Mo	V	Mn	Si	La	S	Fe
Content (wt-%)	0.20	5.60	3.20	2.01	0.35	1.55	0.83	0.30	0.03	balance

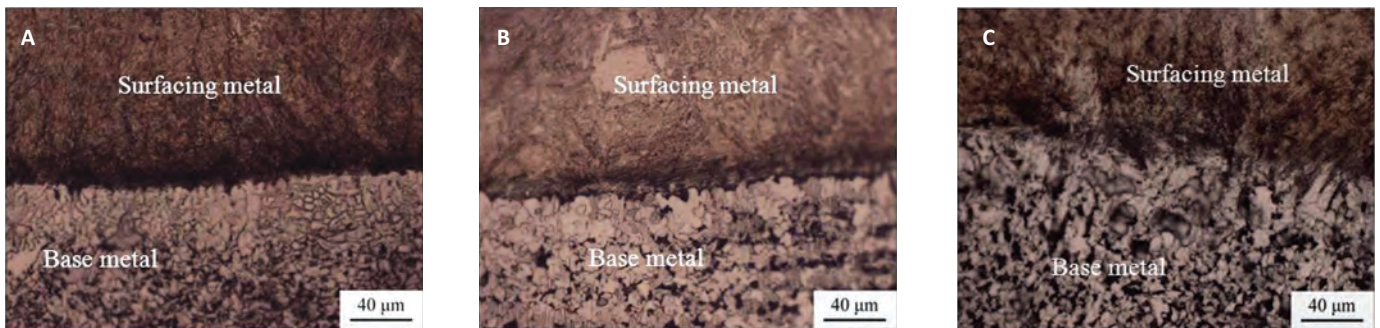


Fig. 3 — Morphologies of the binding profiles with different welding currents. A — 200–220 A; B — 280–300 A; C — 360–380 A.

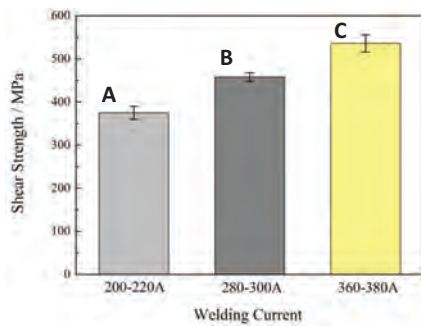


Fig. 4 — Shear strengths between the hardfacing layers and the base metals with different welding currents. A — 200–220 A; B — 280–300 A; C — 360–380 A.

Shear Strength, Hardness, and Wear Resistance Testing

Shear strength between the hardfacing layer and the base metal was determined by an Inspeckt-100 Table electronic universal testing machine. The specimen dimensions are given in Fig. 1. During processing, the tensile rate was set as 1 mm/min.

The macrohardness of the hardfacing layer was measured using an HR-105A Rockwell hardness tester with a load of 150 kg. Subsequently, a wear resistance experiment was carried out on the abrasive belt-type wear tester, in which SiC of 80 mesh was selected as the abrasive material, the wear velocity of the abrasive belt was 1.8×10^4 mm/min, and the applied load was 100 N. Figure 2 shows the photograph and schematic diagram of the abrasive belt-type wear tester (Ref. 13). Electronic balance with accuracy of 0.1 mg was used to weigh the mass loss of the layer per 30 min. After the wear test, the worn surface morphology was observed by a KYKY-2800 scanning electron microscope (SEM).

For the welding joint surface, the

Table 4 — The Amounts of Retained Austenite in the Hardfacing Layers with Different Welding Currents

Welding Currents (A)	200–220	280–300	360–380
Contents (Vol- %)	17.8	11.2	7.1

microhardness along the depth in the profile section of the layer was measured by an FM-700 Vickers hardness tester with a load of 0.2 kg for 10 s. The value presented is the average of five measurements after the highest and lowest values were discarded.

Numerical Simulation and Thermodynamic Calculation

In order to research the effect of welding current on the temperature of the hardfacing molten pool, ANSYS software was applied to simulate the welding temperature field. On the processing, the temperature field module was selected.

Subsequently, CCT curves of the hardfacing layer during the cooling process were calculated by thermodynamic database JMatPro software (Ref. 14) developed by Sente Software, Ltd., UK. During the input data processing, the general steel database was selected as material type, and the chemical composition was inputted according to Table 3.

Results

Welding Associativity

Morphologies of the binding profiles between hardfacing layers and base metals with different welding currents are shown in Fig. 3. Moreover, the shear strengths between the

hardfacing layers and the base metals with different welding currents are given in Fig. 4.

When the welding current is 200–220 A, the hardfacing layer and base metal are not mutually merged, and the weld interface exists between them — Fig. 3A. As seen in Fig. 4, the shear strength between the hardfacing layer and the base metal is 374 MPa.

When the welding current increases to 280–300 A, shown in Fig. 3B, the weld interface still exists, but is significantly widened. Moreover, there are some merge areas appearing between the hardfacing layer and the base metal. Meanwhile, the shear strength increases to 458 MPa.

When the welding current is 360–380 A, the hardfacing layer and base metal merge significantly and the weld interface almost disappears, as shown in Fig. 3C. Moreover, the shear strength between the hardfacing layer and the base metal is the highest at 546 MPa. These results show binding strength between the hardfacing layer and the base metal enhances gradually with the increase in welding current.

Microstructure

Figure 5 displays the optical microscope (OM) morphologies of the hardfacing layers with different welding currents. In Fig. 5A, when the welding current is 200–220 A, the microstructures are composed of short black acicular martensite and retained austenite

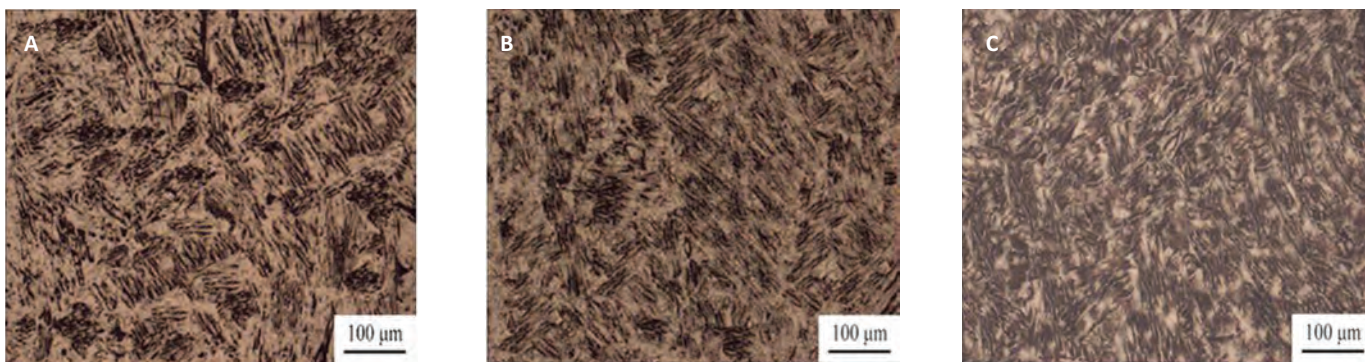


Fig. 5 — Optical microscope morphologies of the hardfacing layers with different welding currents. A — 200–220 A; B — 280–300 A; C — 360–380 A.

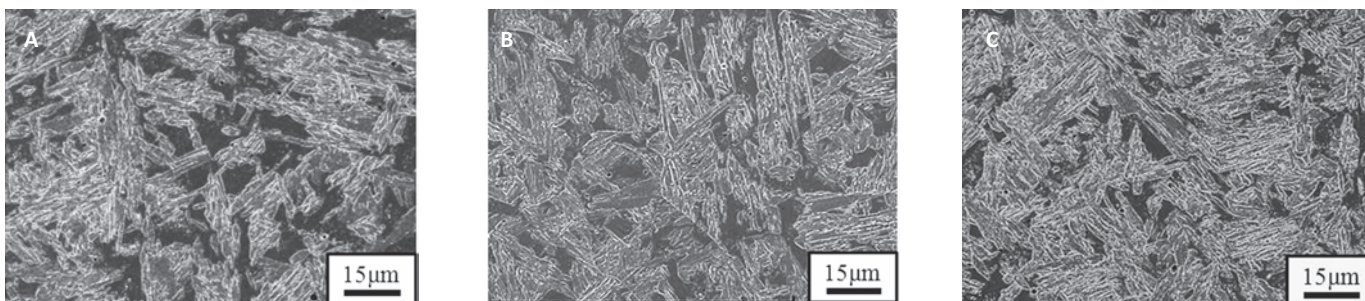


Fig. 6 — Scanning electron microscope morphologies of the hardfacing layers with different welding currents. A — 200–220 A; B — 280–300 A; C — 360–380 A.

ite. With an increase in welding current, shown in Fig. 5B and C, the amount of martensite increases constantly.

Figure 6 shows the scanning electron microscope (SEM) morphologies of the hardfacing layers with different welding currents. Similar conclusions were obtained from these results; with an increase in welding current, the amount of martensite increases constantly. Moreover, there is no change in the martensite morphology.

Figure 7 illustrates the transmission electron microscope (TEM) morphologies of the hardfacing layers with different welding currents, in which, with an increase in welding current, the number of dislocations increases because of the increasing amount of martensite.

The X-ray diffraction (XRD) patterns of the hardfacing layers with different welding currents are shown in Fig. 8. From these results, the authors noted the intensities of martensite (α -Fe) peaks increase, while austenite (γ -Fe) peaks decrease with the increase in welding current. When the welding current reaches 360–380 A, the austenite (γ -Fe) peaks disappear com-

pletely. The amount of retained austenite can be measured according to the XRD patterns (Ref. 15):

$$V_{\gamma} = \frac{1.4I_{\gamma}}{I_{\alpha} + 1.4I_{\gamma}} \quad (1)$$

where V_{γ} is the volume fraction of retained austenite; I_{γ} is the average integrated intensity of austenite diffraction peak of (200) and (311) planes; and I_{α} is the integrated intensity of martensite diffraction peak of (211) plane.

Table 4 lists the amounts of retained austenite in the hardfacing layers with different welding currents. From it, when the welding current increases to 360–380 A from 220 to 220 A, the amounts of retained austenite decrease from 17.8 to 7.1 vol-%. Because of the very low carbon content, the amount of carbide can be ignored, which means the amount of martensite V_M can be approximated as Equation. 2:

$$V_M = 1 - V_{\gamma} \quad (2)$$

Therefore, with the increase in welding current, the amount of martensite in the hardfacing metal in-

creases from 82.2 to 92.9 vol-%, which is consistent with the results in Fig. 5.

Hardness

Figure 9 shows the hardness of the hardfacing layers with different welding currents. When the welding current is 200–220 A, average hardness of the hardfacing layer is HRC 42. With the increasing welding current, hardness of the hardfacing layer increases gradually, and it reaches HRC 45 when the welding current is 360–380 A.

The average lateral microhardness from the base metal to the hardfacing layer is shown in Fig. 10. The value 0 on the x-axis represents the weld interface between the base metal and the hardfacing layer. From Fig. 10, the authors observed the microhardness of the base metal is low. Due to the heat input of the hardfacing, the microhardness of the HAZ increases slightly. Meanwhile, the fusion zone is relatively narrow during the hardfacing process. With an increase in welding current, the microhardness of the hardfacing layer increases. When the welding current is 200–220 A, the lateral microhardness is 422 HV; when the welding current is

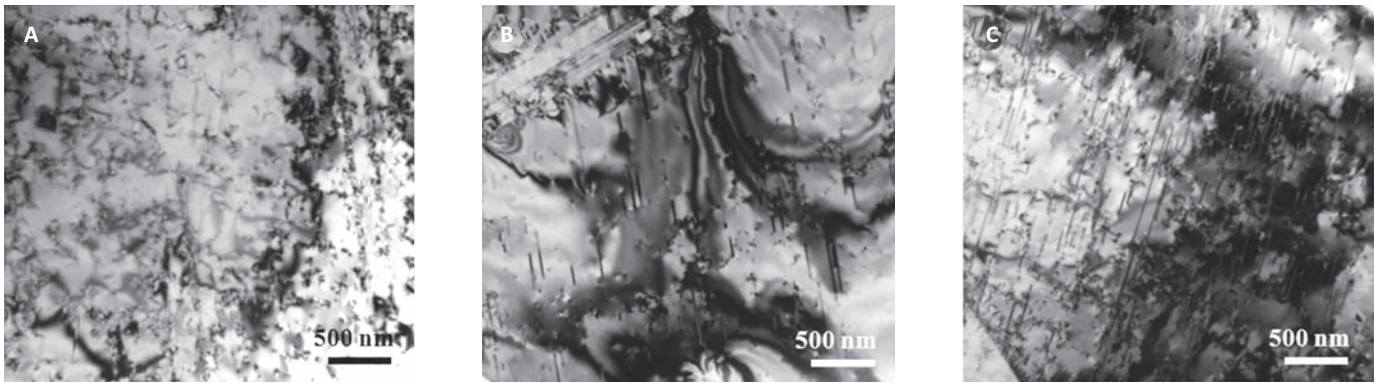


Fig. 7 — Transmission electron microscope morphologies of the hardfacing layers with different welding currents. A — 200–220 A; B — 280–300 A; C — 360–380 A.

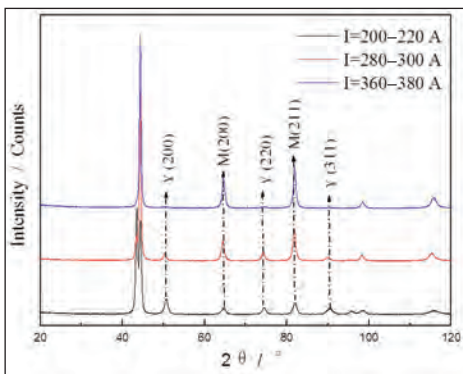


Fig. 8 — X-ray diffraction patterns of the hardfacing layers with different welding currents.

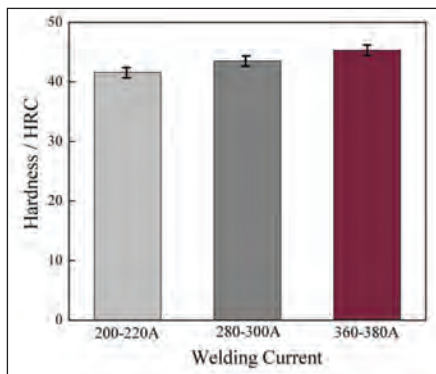


Fig. 9 — Hardness of the hardfacing layers with different welding currents.

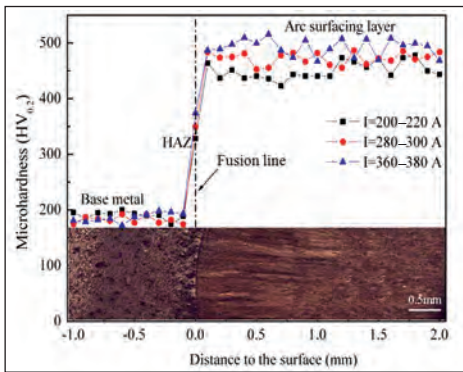


Fig. 10 — Microhardness along the depth-infile section of the arc hardfacing layer.

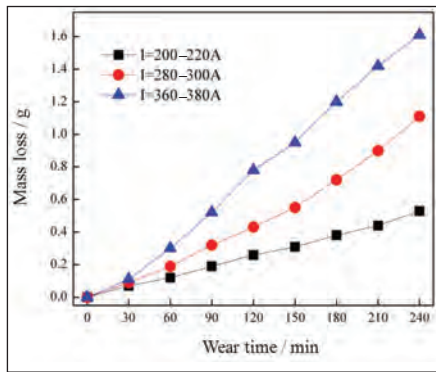


Fig. 11 — Weight loss of the hardfacing layers with different welding currents.

280–300 A, the lateral microhardness increases to 448 HV; when the welding current is 360–380 A, the lateral microhardness is the highest at 480 HV.

Wear Resistance

The weight loss curves of the hardfacing surface layers with different welding currents are shown in Fig. 11. As shown, the weight loss of the hardfacing layer with 200–220 A welding

current is the largest. When the welding current increases to 280–300 A, the wear resistance of the hardfacing layer improves significantly and the wear weight loss reduces. When the welding current is 360–380 A, wear resistance of the hardfacing layer is the highest.

Figure 12 illustrates the wear morphologies of the hardfacing layers with different welding currents tested for 240 min. When the welding current is 200–220 A, surface scratches are both

Table 5 — Thermal Properties of the Hardfacing Layer

Parameter	Value
Molar Mass / $\text{kg}\cdot\text{mol}^{-1}$	55.85
Density / $\text{kg}\cdot\text{m}^{-3}$	6976
Viscosity Coefficient / $\text{Pa}\cdot\text{s}$	0.0063
Specific Heat Capacity / $\text{J}\cdot\text{kg}^{-1}\cdot\text{K}^{-1}$	809
Thermal Conductivity / $\text{W}\cdot\text{m}^{-1}\cdot\text{K}^{-1}$	13.4

wide and deep and flaking exists — Fig. 12A. With the increase in welding current, surface scratches become shallow and narrow. When the welding current increases to 360–380 A, the scratches are the shallowest and narrowest, as shown in Fig. 12C.

Figure 13 shows the XRD patterns of the hardfacing layers with different welding currents after the wear test. Compared with Fig. 8, the amount of retained austenite in the worn hardfacing layer is decreased, while that of martensite is increased. The result indicates strain hardening is occurring during the wearing and influences the wear resistance of the hardfacing layer.

Discussion

The results mentioned previously indicated the hardness and wear resistance of the hardfacing layer both increase with the increase in welding current. To further investigate the mechanism, the effects of the welding current on the hardfacing molten pool temperature and the hardenability of the hardfacing layer were studied.

However, because of the limit of the experimental conditions, it was impossible to directly measure the hardfacing molten pool temperature and the hardenability of the hardfac-

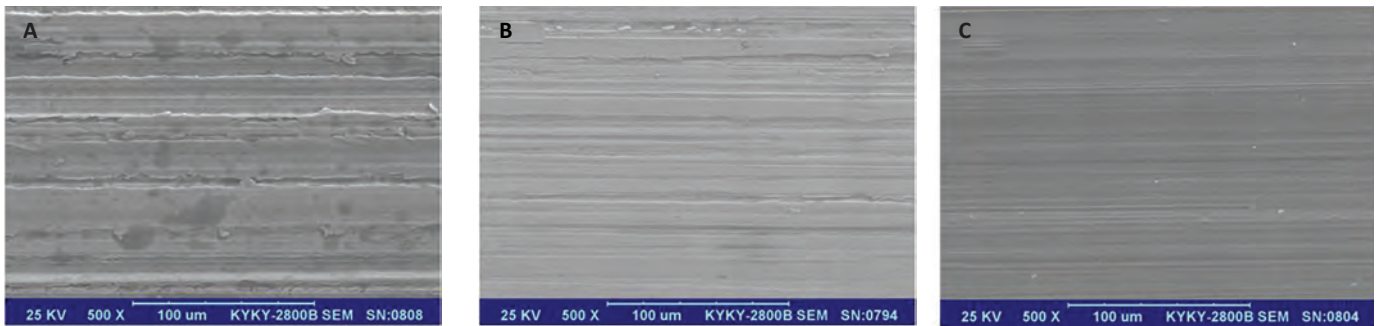


Fig. 12 — Wear morphologies of the hardfacing layers with different welding currents tested for 240 min. A — 200–220 A; B — 280–300 A; C — 360–380 A.

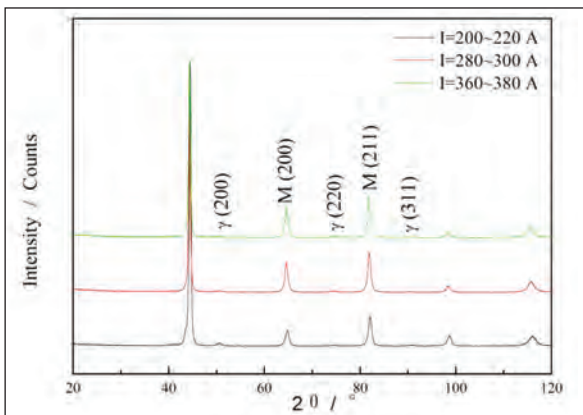


Fig. 13 — X-ray diffraction patterns of the hardfacing layers with different welding currents after wear test.

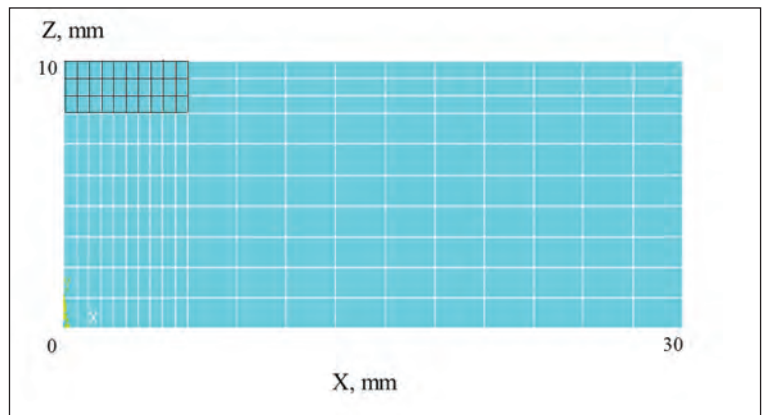


Fig. 14 — Element division of the calculated specimen.

ing layer. Therefore, ANSYS and JMat-Pro calculation softwares were selected to calculate, respectively, the hardfacing molten pool temperature and simulate the CCT curves of the hardfacing layers during the cooling process.

ANSYS Results

Heat Source Selection

The effect of welding current on the hardfacing molten pool temperature was simulated by ANSYS software. This work only concerned itself with the relationship between the welding current and the hardfacing molten pool temperature. The other factors, such as welding speed and welding direction, were ignored. Because of the small computational amount and the high computational accuracy, the Gaussian heat source model was used, in which heat flux of point *P* is shown as Equation 3 (Ref. 16):

$$q_r = \frac{3\eta UI}{\pi R^2} \exp\left(-\frac{3r^2}{R^2}\right) \quad (3)$$

where *R* is the effective heating radius of the arc; *h* is the welding thermal efficiency; *U* and *I* are welding voltage and welding current, respectively; and *r* is the distance between *P* to arc center.

Model Building and Thermal Properties

The tested specimen used for calculation was made of the hardfacing layer metal with the dimensions 60 × 20 mm. During the simulation process, the temperature fields can be treated as the axial symmetry. Therefore, in order to reduce the calculation amount, the calculated specimen was halved, as shown in Fig. 14. The specimen was divided into 200 elements and 231 nodes, and the hardfacing region is shown by the dotted lines — Fig. 14. Thermal properties of the hardfacing layer are listed in Table 5.

Boundary Conditions

The heat transfer control equation of the welding process is given as follows:

$$\rho c \frac{\partial T}{\partial t} = \frac{\partial}{\partial x} \left(\lambda \frac{\partial T}{\partial x} \right) + \frac{\partial}{\partial y} \left(\lambda \frac{\partial T}{\partial y} \right) + \frac{\partial}{\partial z} \left(\lambda \frac{\partial T}{\partial z} \right) + Q \quad (4)$$

where *ρ* and *c* are specific heat capacity and density of the material, *T* is the temperature, *t* is the time, *Q* is the heat source, and *λ* is the thermal conductivity. Moreover, *X*, *Y*, and *Z* are the coordinate axes.

The boundary conditions applied during the ANSYS modeling can be divided into upper surface boundary condition, lateral and lower surface ones, and the *Y* axis symmetry plane.

For the upper surface, because the Gaussian heat source model was used, the model cross section in the *Z* direction is round, and heat-flux density on the cross section obeys Gauss distribution. Moreover, heat-flow density values are the same in all parts of the *Z* axis. The specific boundary condition is given as follows:

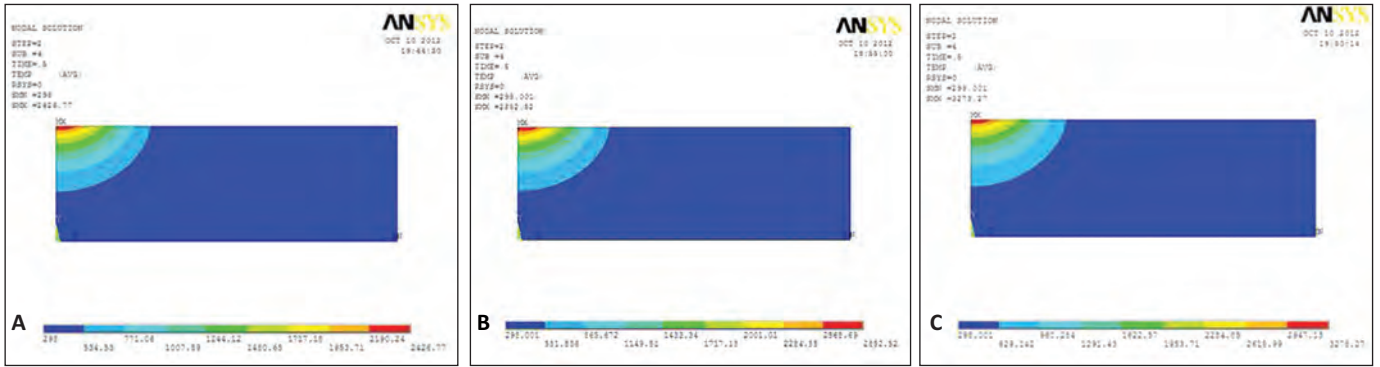


Fig. 15 — Molten pool temperatures of the hardfacing layers with different welding currents. A — 200–220 A; B — 280–300 A; C — 360–380 A.

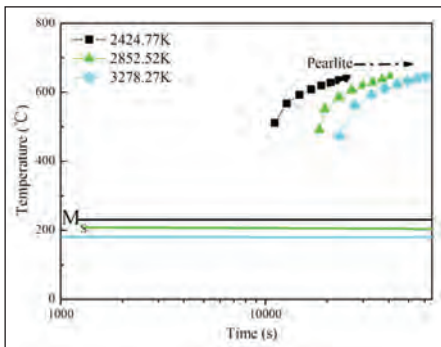


Fig. 16 — CCT curves of the hardfacing layers with different welding currents.

$$q(x, y, z) = \frac{3C_s Q}{\pi H \left(1 - \frac{1}{e^3}\right)} \exp \left[\frac{-3C_s}{\log \left(\frac{H}{z}\right)} (x^2 + y^2) \right] \quad (5)$$

where C_s is the heat source focus coefficient, $C_s = 3/R_0^2$, R_0 is the heat source opening radius, H is the heat source height, and Q is the heat source power.

During processing, heat is lost in the forms of thermal convection and thermal radiation. The boundary condition is shown in Eq. 6:

$$-K \frac{\partial T}{\partial Z} = -h_c (T - T_a) - \sigma \varepsilon \{T^4 - T_a^4\} \quad (6)$$

where h_c is the convection coefficient, S is the Stefan-Boltzman constant, e is

the surface thermal emission rate, and T_a is the room temperature.

For the lateral and lower surfaces, the boundary condition is

$$\lambda \frac{\partial T}{\partial n} = -q + \alpha (T - T_0) \quad (7)$$

$$\alpha = \alpha_c + \alpha_r \quad (8)$$

where α is the total heat transfer coefficient, α_c is the thermal convection coefficient, and α_r is the thermal radiation coefficient.

For the Y axis symmetry plane surface, the boundary conditions are shown as follows:

$$\frac{\partial T}{\partial y} = 0, \quad \frac{\partial u}{\partial y} = 0, \quad \frac{\partial w}{\partial y} = 0, \quad v = 0 \quad (9)$$

Simulation Results

Figure 15 shows the molten pool temperatures of the hardfacing layers with different welding currents. When the welding current is 200–220 A, molten pool temperature is 2424.77 K — Fig. 15A. With an increase in welding current, the molten pool temperature increases. When the welding current is 360–380 A, the molten pool temperature is the highest at 3278.27 K — Fig. 15C.

JmatPro Results

The CCT curves calculation by the JmatPro software follows the general equation established by Kirkaldy (Ref. 17):

$$\tau(x, T) = \frac{I}{\alpha D \Delta T^q} \int_0^x \frac{d_x}{x^{2(1-x)/3} (1-x)^{2x/3}} \quad (10)$$

where $a = \beta 2^{(G-1)/2}$, β is an empirical coefficient, G is the ASTM grain size, D is an effective diffusion coefficient, ΔT is the undercooling, and q is an exponent.

Figure 16 shows the CCT curves of the hardfacing layers during the cooling process. With the increase of the molten pool temperature, the pearlite phase region moves to the right, and the martensitic transition start temperature M_s decreases constantly — Fig. 16. When the molten pool temperature increases from 2424.77 to 3278.27 K, the martensitic transition start temperature M_s decreases from 243.7° to 174.1° C.

The reason is, when the molten pool temperature (austenitizing temperature) is high, the cementite dissolution and austenitic homogenization are promoted, and the austenite grain is coarsened. Therefore, the formation of the pearlite is delayed, which causes the pearlite phase region to move to the right. At the same time, the grain becomes coarse and dissolved carbide increases, so the carbon content of austenite increases, which decreases the M_s temperature (Ref. 18).

The rightward motion of the pearlite phase region and the decreasing martensitic transition start temperature in the CCT curve both illustrate the increase in hardenability of the hardfacing layer, which then caus-

es the amount of martensite to increase. The CCT curves show that with the increase in welding current, the molten pool temperature of the hardfacing layer increases, which leads to the increase in hardenability. So, the amount of hard martensite increases while the soft retained austenite decreases. Therefore, the hardness and wear resistance both increase with the increase in welding current.

Conclusion

The effects of flux cored arc welding current on the microstructure, wear resistance, and welding associativity of the hardfacing layer were investigated in this work. The results are as follows:

1. Binding strength between the hardfacing layer and the base metal enhances gradually with the increase in welding current. When the welding current reaches 360–380 A, the binding strength is the highest.

2. With the increase in welding current, the molten pool temperature of the hardfacing layer increases from 2424.77 to 3278.27 K, which makes the pearlite phase region move to the right and the martensitic transition start temperature M_s decrease (from 243.7° to 174.1°C) during the cooling process, which then improves the hardenability of the hardfacing layer.

3. With the increase in welding current, the amount of martensite in the hardfacing layer increases while that of retained austenite decreases, which leads to the increase in hardness and wear resistance.

4. After wear test, the amounts of retained austenite in all of the hardfacing layers are lowered, while those of martensite are increased. This indicates that strain hardening occurs dur-

ing the wearing, and then affects the wear resistance of the hardfacing layer.

References

1. Ding, H., Hirai, K., and Kamado, S. 2010. Microstructure characteristics during the multi-pass hot rolling and their effect on the mechanical properties of AM50 magnesium alloy sheet. *Materials Science and Engineering A* 527(15): 3379–3385.
2. Zhang, Z., Wang, M. P., Zhu, S., and Jiang, N. 2012. Preferential dynamic recrystallization at original grain boundaries in the hot-rolling process of AZ31 alloy. *Journal of Alloys and Compounds* 544: 159–165.
3. Yang, J., Zhang, P. F., Zhou, Y. F., Xing, X. L., Ren, X. J., Yang, Y. L., and Yang, Q. X. 2014. Mechanical properties of the hardfacing alloys with different La_2O_3 additives and the mechanism analysis by first-principles calculations. *Materials Science & Engineering A* 591: 82–89.
4. Katsich, C., and Badisch, E. 2011. Effect of carbide degradation in a Ni-based hardfacing under abrasive and combined impact/abrasive conditions. *Surface and Coatings Technology* 206(6): 1062–1068.
5. Sterjovski, Z., Pitrun, M., Nolan, D., Dunne, D., and Norrish, J. 2007. Artificial neural networks for predicting diffusible hydrogen content and cracking susceptibility in rutile flux-cored arc welds. *Journal of Materials Processing Technology* 184(1): 420–427.
6. Jenkins, N. T., Pierce, W. M. G., and Eagar, T. W. 2005. Particle size distribution of gas metal and flux cored arc welding fumes. *Welding Journal* 84(10): 156-s to 163-s.
7. Jackson, C. E., and Shrubbsall, A. E. 1953. Control of penetration and melting rate with welding technique. *Welding Journal* 32(4): 172-s to 178-s.
8. Gunaraj, V., and Murugun, N. 1999. Prediction and comparison of area of heat affected zone for bead on plate and bead on joint in submerged arc welding of pipes. *Journal of Materials Engineering and Performance* 95(1): 246–261.
9. Kannan, T., and Yoganandh, J. 2010. Effect of process parameters on clad bead geometry and its shape relationships of stainless steel claddings deposited by GMAW. *The International Journal of Advanced Manufacturing Technology* 47(9–12): 1083–1095.
10. Gualco, A., Svoboda, H. G., Surian, E. S., and de Vedia, L. A. 2010. Effect of welding procedure on wear behaviour of a modified martensitic tool steel hardfacing deposit. *Materials & Design* 31(9): 4165–4173.
11. Buchanan, V. E. 2009. Solidification and microstructural characterization of iron–chromium based hardfaced coatings deposited by SMAW and electric arc spraying. *Surface and Coatings Technology* 203(23): 3638–3646.
12. Karaoğlu, S., and Secgin, A. 2008. Sensitivity analysis of submerged arc welding process parameters. *Journal of Materials Processing Technology* 202(1): 500–507.
13. Yang, J., Yang, Y. L., Zhou, Y. F., Qi, X. W., Gao, Y. K., Ren, X. J., and Yang, Q. X. 2013. Microstructure and wear properties of Fe-2wt-% Cr-X wt-% W-0.67 wt-% C hardfacing layer. *Welding Journal* 92(8): 225-s to 230-s.
14. Saunders, N., Guo, U. K. Z., Li, X., Miodownik, A. P., and Schillig, J. P. 2003. Using JMatPro to model materials properties and behavior. *JOM* 55(12): 60–65.
15. Wang, L. J., Cai, Q. W., Yu, W., Wu, H. B., and Lei, A. D. 2010. Microstructures and mechanical properties of 1500 MPa ultra-high strength low alloy steel. *Metal Journal* 46(6): 687–694.
16. Rouquette, S., Guo, J., and Le Masson, P. 2007. Estimation of the parameters of a Gaussian heat source by the Levenberg-Marquardt method: Application to the electron beam welding. *International Journal of Thermal Sciences* 46(2): 128–138.
17. Kirkaldy, J. S., and Sharma, R. C. 1982. A new phenomenology for steel IT and CCT curves. *Scripta Metallurgica* 16(10): 1193–1198.
18. Zhao, P., Xie, F. Z., and Sun, Z. G. 2006. *Materials science basic tutorial*. Harbin: Harbin Institute of Technology Press.